J. Fluid Mech. (1994), *vol.* 267, *pp.* 275–298

Turbulent mixing at an inversion layer

By M. J. A. M. PERERA, H. J. S. FERNANDO AND D. L. BOYER

Program in Environmental Fluid Dynamics, Department of Mechanical and Aerospace Engineering, Arizona State University, Tempe, AZ 85287–6106, USA

(Received 28 April 1992 and in revised form 18 October 1993)

A series of laboratory experiments was carried out to examine the interaction between stratification and turbulence at an inversion layer, with the objective of gaining insight into certain wave–turbulence encounters in the atmosphere. A three-layer stratified fluid system, consisting of a (thick) strongly stratified inversion layer, sandwiched between an upper turbulent layer and a lower non-turbulent weakly stratified layer, was employed. Oscillating-grid-induced shear-free turbulence was used in the upper layer. During the experiments, a fourth (interfacial) layer developed in the region between the inversion and the turbulent layer, and most of the wave–turbulence interactions were confined to this layer. Detailed measurements of the vertical velocity structure, internal-wave parameters and mixing characteristics were made in the stratified layers and, whenever possible, the results were compared to available theoretical predictions.

1. Introduction

There are many flow situations where the boundaries of a turbulent region are stably stratified layers. These boundary regions may be either non-turbulent or turbulent, the latter characterized by localized areas within which turbulence is sporadically generated and rapidly decayed. In general, turbulence forcing at the boundary between turbulent and stratified layers (called the entrainment interface) can generate internal waves which may break at or in the neighbourhood of the interface, causing localized turbulent patches. Waves can also be radiated into the outer stratified layer, carrying energy out of the turbulent layer. Breaking of internal waves can be attributed to a variety of mechanisms including forced resonance, internal strain, convective instabilities, resonant interactions, critical-layer absorption, or a combination thereof.

The structure of turbulence at or near density inversions as well as the motion within the interior of the stratified layers are of interest in aiding better understanding of such phenomena as mixed-layer growth and pollutant dispersion. An example is the evolution of the atmospheric convective boundary layer (CBL) during the day-time heating of the ground. In modelling such situations, a three-layer structure is assumed for the lower atmosphere; the bottom layer near the surface (CBL) is well mixed (up to the mixing height) by the convective turbulence, and the outer weakly stratified layer is separated from the CBL by a strongly stable, relatively thin, inversion layer (for a discussion, see Grisogono & Keislar 1992). Thus the buoyancy-frequency profile in the lower atmosphere can be approximated as

$$N(z) = \begin{cases} 0 & \text{for} \quad 0 < \zeta < h_1, \\ N_i & \text{for} \quad h_1 < \zeta < h_1 + h, \\ N_u & \text{for} \quad h_1 + h < \zeta < h_1 + h + h_2, \end{cases} \tag{1.1}$$

where ζ is the vertical coordinate measured from the ground, h_1 the mixing height, N_i the buoyancy frequency within the inversion of thickness h, and N_u ($< N_i$) the buoyancy frequency of the weakly stratified layer of thickness h_2. Mixing at the entrainment interface leads to the growth of the mixing height, and the mixing mechanism can be one of the following:

(i) at very low interfacial stabilities, the turbulent eddies of the mixed layer can engulf inversion-layer fluid, as if there were no stratification (Townsend 1976);

(ii) at low stabilities, the eddies can impinge on the interface and splash the non-turbulent fluid into the mixed layer, as proposed by Linden (1973), or thin sheets of inversion-layer fluid can be scoured by eddies sloshing over the interface;

(iii) at moderate stabilities, internal waves in the inversion can break and cause isolated mixed regions that eventually merge with the mixed layer (Fernando & Long 1983); and,

(iv) at high stabilities, the entrainment process can be dominated by molecular-diffusive effects (Crapper & Linden 1974).

The parameter ranges over which these mechanisms are operative depend on the nature of the turbulence and stratification. The turbulence beneath an atmospheric inversion depends on the time of the day and the season, among other factors. Numerical simulations of Deardorff (1980) show that, during the day-time, the shear-generated turbulence in the CBL is overshadowed by the (mean shear-free) convective turbulence. At night, of course, the shear-induced turbulence is the sole energy production mechanism. Although a three-layer stratification is common in the ocean, it has been found that, at least in equatorial regions, the shear production at the base of the mixed layer is important at all times (Moum, Caldwell & Paulson 1989).

The present work deals with the interaction of shear-free turbulence and stratification in a three-layer system similar to (1.1). For experimental convenience, the upper layer is maintained turbulent and the layers below are stably stratified; the shear-free turbulence is induced by an oscillating grid. A schematic of the experimental apparatus is shown in figure 1 (*a*) and the stratification is shown in figure 1 (*b*) (further discussion of this system will be given later). Based on linear internal wave theory, one should expect that waves generated at the inversion have frequencies ω satisfying $\omega < N_i$ and that waves radiated into the outer layer have frequencies $\omega < N_u$. Since $N_i > N_u$, it is further expected that waves in the inversion satisfying $N_u < \omega < N_i$ will be trapped within and, owing to the build up of energy, break, thus dissipating energy. The resulting localized mixing should lead to a reduction of the buoyancy gradient within the interface and to the thickening of the turbulent layer.

The external governing parameters for the problem in hand are the buoyancy frequencies of the stratification N_i and N_u, the thickness of the inversion h, the integral lengthscale L_H and the r.m.s. horizontal velocity u_H of turbulence (note that L_H and u_H corresponding to measures of the background turbulence that would be obtained at the location of the interface, but in its absence – for details see Carruthers & Hunt 1986). The governing dimensionless parameters can be identified as:

$$\left.\begin{aligned} &\text{Bulk Richardson number} \quad Ri = N_i^2 L_H^2/u_H^2, \\ &\text{Internal Richardson number} \quad Ri_I = N_i^2 h^2/u_H^2, \\ &\text{and} \quad \text{Frequency ratio} \quad \epsilon = N_u/N_i. \end{aligned}\right\} \tag{1.2}$$

(Sometimes it is advantageous to use $Ri_\Delta = \Delta b L_H/u_H^2$ based on the buoyancy jump across the inversion Δb, instead of Ri). Carruthers & Hunt (1994) and Fernando &

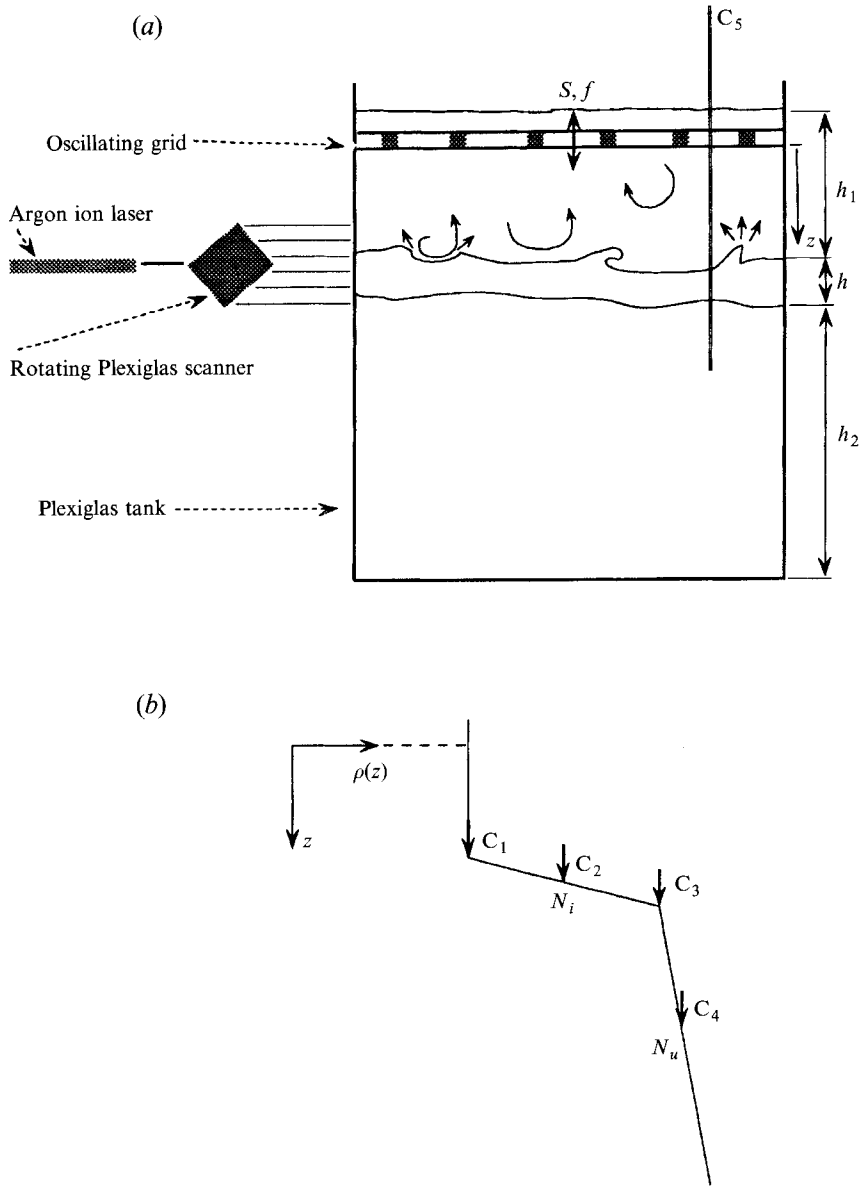

FIGURE 1. (*a*) A schematic of the experimental apparatus, and (*b*) the three-layer stratification used for the experiment. The positions of the conductivity probes are given by C_1, C_2, C_3 and C_4, and the traversing conductivity probe is designated C_5.

Hunt (1994) have delineated the relative roles played by the two Richardson numbers Ri and Ri_I. They showed that the wave motion in the inversion is governed by Ri_I, whereas the suppression of turbulent diffusion at the interface is determined by Ri. When $Ri_I < \pi^2$, which is typical of thin interfaces, the inversion can only sustain the first mode of internal waves ('flapping' mode). When $Ri_I > \pi^2$ (thick interfaces), higher modes are possible, yielding a complex motion field with trapped waves. This raises the important question: for given L_H, u_H and N_i, can the entrainment rate at a thick inversion be the same as that of a thin interface? The internal-wave energy radiation to the outer layer is an obvious determining factor, but previous studies indicate that

it is negligible (E & Hopfinger 1986). Another key consideration should be the structure of the wave field and associated energetics; for the two cases, they are different and suggest the possibility of different mixing rates. Most laboratory data thus far reported fall into the category of $Ri_J < \pi^2$ and inspection of the available atmospheric boundary-layer data suggests that they belong to $Ri_J > \pi^2$ (Deardorff 1980). The issue of whether higher modes of trapped internal waves actually exist or, even if they do, whether they make a contribution toward mixing at the tropopause has not been resolved (Caughey, Crease & Roach 1982; Scott & Kerry 1985; Gossard *et al.* 1982). The aim of the present work is to address such issues using laboratory experiments. In particular, the work was motivated by the following reasons.

(i) It is important that previous oscillating-grid-driven mixing-box experiments be extended to three-layer configurations that permit the development of higher modes of internal waves. If the experiments were to start with either a two-layer fluid or a linearly stratified fluid, the resulting inversion will be thin and higher internal-wave modes will be absent. Further, previous laboratory experiments related to lower-atmospheric mixing performed by heating a linearly (heat) stratified fluid from below (Deardorff, Willis & Stockton 1980; Heidt 1977), have been unsuccessful in producing an interfacial stratification similar to that of the atmosphere (Turner 1991).

(ii) Although a comprehensive set of measurements exist for mixing in two-fluid systems subjected to shear-free turbulence (Hannoun & List 1988; Fleury *et al.* 1990), no corresponding measurements are available for linearly stratified fluids.

(iii) There is a comprehensive series of recent theoretical predictions on the nature of turbulence near density interfaces (see Carruthers & Hunt 1986, 1994, henceforth referred to as CH1 and CH2, respectively). These theories are based mainly on well-founded assumptions, and can form the basis of interpretation for the present measurements. Useful summaries and discussion of these papers are given in Carruthers, Hunt & Turfus (1986) and Carruthers & Moeng (1987), and a brief review of CH2 is given in §2. In CH1, the response of an unbounded stratified fluid layer, neighbouring a shear-free turbulent layer, was considered; no inversion was present ($h = N_i = 0$). An inversion was introduced in CH2, so as to produce a flow configuration similar to (1.1). Although the predictions of CH2 have shown qualitative agreement with the large-eddy simulation results of Carruthers & Moeng (1987) and some atmospheric observations (Caughey & Kitchen 1984), there are other observations that are at variance with the predictions (Caughey *et al.* 1982). Thus, it is instructive to verify the theoretical predictions in the laboratory. E & Hopfinger (1986) have attempted to compare their laboratory measurements with CH1; development of an interfacial layer in their experiments, however, suggests that such a comparison may be incongruous.

This paper is arranged as follows. Section 2 is devoted to a discussion of some features of CH2, predictions of which are central to this paper. In §3, the experimental procedure is discussed. The results of the experiments are given in §4 and a summary and discussion of the experimental findings are given in §5.

2. An outline of the CH2 theory

Because of the concomitance between CH2 and the present work, it is instructive to outline the basis and some salient results of the former. In developing this theory, the flows in the three layers were considered separately and appropriate interfacial matching conditions were employed. The major steps used are as follows.

(i) The turbulence in the interior of the mixed layer is assumed to be homogeneous and isotropic, specified by the joint wavenumber ($\boldsymbol{k}$) frequency (ω) spectra

$$X_{ij}^{H}(\boldsymbol{k},\omega) = \int_{-\infty}^{+\infty}\iint \overline{u_i^H(\boldsymbol{x}+\boldsymbol{r},t+\tau)\,u_j^H(\boldsymbol{x},t)}\,\mathrm{e}^{-\mathrm{i}(\boldsymbol{k}\cdot\boldsymbol{r}-\omega\tau)}\,\mathrm{d}\tau\,\mathrm{d}\boldsymbol{r}, \tag{2.1}$$

where u_i^H is the velocity fluctuation and $\boldsymbol{r}$ and τ are space and time separations, respectively. On the basis of the atmospheric field observations of Kaimal *et al.* (1976) that the rate of dissipation of turbulent kinetic energy is constant with ζ near the inversion zone, it was inferred that $\mathrm{d}\overline{\Omega^2}/\mathrm{d}\zeta = 0$, where $\overline{\Omega^2}$ is the mean square vorticity fluctuation. This implies that the introduction of an inversion into a homogeneous turbulent layer can be treated as an irrotational perturbation, and hence the velocity field near the interface is given by

$$\boldsymbol{u} = \boldsymbol{u}^H - \nabla\phi, \tag{2.2}$$

where ϕ is the velocity potential and $\nabla^2\phi = 0$.

A model proposed by CH1, which takes into consideration the advection of smaller eddies by eddies of the integral lengthscale, was used for $X_{ij}^H(\boldsymbol{k},\omega)$, namely

$$X_{ij}^H(\boldsymbol{k},\omega) = \Phi_{ij}^H(\boldsymbol{k})\,\delta(\omega - u_H k), \tag{2.3}$$

where $\Phi_{ij}^H(\boldsymbol{k})$ is the three-dimensional spectral tensor and $k = |\boldsymbol{k}|$ is the magnitude of the wavenumber. The semi-empirical formulations proposed by von Kármán or Townsend were used for $\Phi_{ij}^H(\boldsymbol{k})$; see CH1.

(ii) The fluid motions within the stratified layers were described using the linear internal-wave equations

$$\frac{\partial^2}{\partial t^2}(\nabla^2 u_3) + N^2\nabla_h^2 u_3 = 0, \tag{2.4}$$

$$\rho\frac{\partial u_i}{\partial t} + \frac{\partial p}{\partial x_i} = 0, \quad i = 1,2, \tag{2.5}$$

and

$$\rho\frac{\partial^2 u_3}{\partial z\,\partial t} = \nabla_h^2 p, \tag{2.6}$$

where u_i is the velocity, t is the time, N is the buoyancy frequency, ρ is the density, z is the vertical coordinate and p is the pressure. Rayleigh friction was introduced to these equations to account for the dissipation of kinetic energy in the (middle) inversion layer, so that there is no unwarranted build-up of wave energy in that layer. The magnitude of friction was such that the r.m.s. wave amplitude, specified by the displacement of isopycnals ξ, is just sufficient to satisfy a criterion for convective instabilities. This effectively models the energetics of the inversion, and allows one to estimate the amount of energy transferred to an inversion layer which sustains a quasi-steady saturated field of internal waves; the wave-energy flux radiated into the outer layer can also be calculated.

(iii) At the interfaces between different layers, the continuity of the vertical velocity ($u_3 = w$) and pressure (p) is assumed (this implies that $\mathrm{d}w/\mathrm{d}z$ is continuous). At $z \to \infty$, the radiation condition was applied for wave frequencies $\omega < N_u$ and $w \to 0$ was used for $\omega > N_u$.

The predictions included the three-dimensional power spectra, velocity variances and integral lengthscales in the layers, and wave properties in stratified layers such as

the wave-energy flux, the isopycnal displacements, the dominant (resonant) frequencies and the variances of the density and buoyancy fluctuations. In what follows attempts will be made to compare these predictions to the experimental results.

3. Experimental procedure and instrumentation

3.1. *Apparatus*

The experiments were carried out in a Plexiglas tank of cross-section 40×40 cm and height 60 cm. The tank was filled to a depth of 55 cm, with a three-layer stratified fluids system, as shown in figure 1(*a*). The turbulence-generating mono-planar grid was positioned horizontally, 51 cm above the bottom of the tank. The grid construction utilized square Plexiglas bars of cross-section 1×1 cm and a mesh size of 4.8 cm; the solidity of the grid was 36%. The grid was mounted to a template located above the water surface by four steel rods of 3 mm diameter. The template was oscillated vertically using a slider crank mechanism, which in turn converted the rotary motion of a high-traction motor to the reciprocating motion of the grid. Oscillating frequencies between 2 and 5 Hz were selected and the stroke was set at 2.6 cm.

The three-layer stratification shown in figure 1(*b*) was obtained using a mixture of aqueous salt and alcohol solutions. The alcohol and salt concentrations were chosen in order to match the refractive indices of the three layers, thus obtaining an optically homogeneous, density-stratified, medium suitable for laser diagnostics. The salt–alcohol refractive-index matching procedure is described in detail by Hannoun, Fernando & List (1988). The technique employed was a modification of the well-known Oster & Yamamoto (1963) method. An aqueous alcohol solution of uniform density (solution A) was prepared and a pre-determined amount was first added to the test cell. Then a mixture emanating from the two-tank system was slowly fed from a capped hole in the bottom of the test cell: the low-density (feeding) tank of the two-tank system initially contained solution A and the high-density tank contained a salt solution of predetermined density. After the required amount of mixture had been fed to obtain the inversion, the liquid in the dense tank was diluted using solution A and the feeding continued to obtain the weakly stratified layer. A minute amount of Rhodamine 6G dye was added to the salt-water tank to establish a passive dye-tracer gradient proportional to the gradient of salt. Because of the high vapour pressure of alcohol, the tanks were covered to minimize evaporation. Owing to the constraints imposed by the requirement of uniform refractivity index, the strengths of the stratifications that could be achieved were limited.

The density stratification was measured using a calibrated microscale conductivity probe attached to a vertically traversing platform; the conductivity and the position of the probe were obtained as analog voltages, and were used to calculate density profiles $\rho(z)$ using standard calibration and automated data handling procedures. A typical initial density profile so obtained is shown in figure 2. The internal-wave fields within the stratified layers were also detected using adjustable stationary conductivity probes; the location of the probes are shown in figure 1(*b*), and are as follows: Probe C_1, entrainment interface; Probe C_2, middle of the inversion layer; Probe C_3, interface between the inversion layer and the outer stratified layer; and Probe C_4, middle of the outer layer.

Positioning of these probes was done following the measurement of vertical density profiles using the traversing probe C_5. Although the transition from one layer to another is depicted as sharp in figure 1(*b*), in practice the transitions were somewhat diffused as a result of mixing that occurred during the filling process (figure 2). In

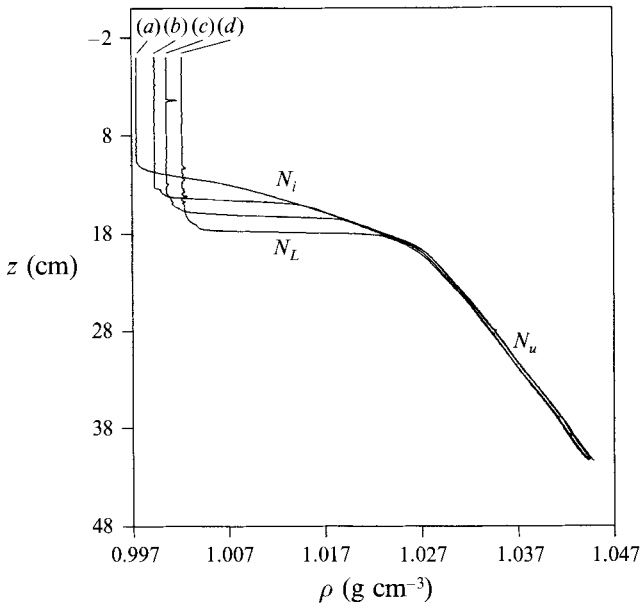

FIGURE 2. Time sequence of density profiles: (*a*) initial profile at $t = 0$, $Ri = 17$; (*b*) $t = 30$ min, (*c*) $t = 120$ min, (*d*) $t = 300$ min.

addition, during the experiments, a (thin) layer having a strong buoyancy gradient N_L ($> N_i$) is developed between the inversion layer and the upper turbulent layer; the probe C_1 was placed in the middle (averaged) of this fourth layer.

3.2. *Concentration measurements using laser-induced fluorescence*

Laser-induced fluorescence (LIF) was used for concentration measurements. This technique is being widely used in mixing studies (Hannoun & List 1988) and is based on the ability of an aqueous Rhodamine 6G dye solution to fluoresce at a wavelength of 570 nm when exposed to Argon-ion laser light of wavelength 514 nm. If a high-pass filter with a cutoff wavelength of 550 nm is used to collect the light into an optical module, the intensity of the fluoresced light is proportional to the dye concentration. The light intensity is attenuated along the optical path due to absorption by the dye; hence very low dye concentrations (less than 200 p.p.b.) must be used.

A columnar laser beam from a 2W Argon-ion laser was directed horizontally toward a rapidly rotating Plexiglas body of square cross-section having dimensions $14 \times 14 \times 2.2$ cm. The faces of the Plexiglas were precision ground and polished. The body was rigidly mounted on a rod passing through the body axis of its short dimension and spun at a constant speed of 1685 r.p.m. To prevent optical distortions introduced by sharp edges, the four corners of the rotor were masked with black tape. Owing to the rapid rotation employed, a vertically scanning field of horizontal parallel rays (of thickness 0.6 mm) was generated. The details of this instrument are given in DeSilva, Montenegro & Fernando (1990).

The scanning light sheet was adjusted to illuminate a region 7 cm in thickness, including the entrainment interface. The fluoresced light, after passing through a high-pass optical filter, was collected on a 512×512 pixel array of a video camera; the sampling rate was 30 frames per s. The video images were collected and processed using a digital image processing board. As each frame was read from the VCR, the pixel

intensities were digitized and saved in the magnetic memory for further processing. In order to better visualize the spatial dye concentration (or the concentration-gradient) distribution, pseudocolour images were created by assigning colours based on grey scales. The intensities of the processed images were scaled by the intensity of the specified largest concentration (or the concentration gradient) so as to create a full contrast image; the maximum concentration (gradient) is assigned the colour blue, the regions of zero concentration (gradient) are assigned the colour red, and the intermediate concentrations (gradients) are assigned intermediate colours, depending on the linear interpolation of grey scales ranging from 0 to 255 (see figure 3*e*, plate 1). Since the variation of the dye concentration below the interface was much smaller than that through the interface, the image enhancement process used to highlight interfacial mixing events displayed the region below the interface as one having uniform colour.

3.3. *Parameterization of turbulence*

It is fortunate that the governing turbulent quantities, u_H and L_H, can be measured in homogeneous fluids and then applied to the stratified system. Extensive work has been reported on the measurement of turbulence in homogeneous fluids; for an excellent review see Hopfinger & Linden (1982). Measurements of the horizontal velocity u_H generally agree with a formula proposed by Hopfinger & Toly (1976), namely

$$u_H/(fS) = \alpha_1 S^{\frac{1}{2}} M^{\frac{1}{2}} z^{-1}, \tag{3.1}$$

where S and f are the stroke and the frequency (in Hz) of grid oscillations, respectively, M is the mesh size, z is the distance from the virtual origin (which is located at a distance $(0.5S+1.5)$ cm above the bottom dead centre of the grid) and α_1 is a constant which is somewhat sensitive to the stroke and the mesh size. For example, Thompson & Turner (1975) found $\alpha_1 \approx 0.2$ for $S = 1$ cm, whereas Hopfinger & Toly (1976) reported $\alpha_1 \approx 0.3$ for $S = 4$ cm. The formula (3.1) is reported to be valid for $M/d < 5$, $f < 6$ Hz and solidity $< 40\%$, all of which are satisfied by the grid used in the present experiments; here d is the width of the grid bars.

Measurements of the r.m.s. vertical velocity w_H and the integral lengthscale L_H show

$$w_H = \alpha_2 u_H, \tag{3.2}$$

where $\alpha_2 \approx 1.25$, and

$$L_H = \alpha_3 z, \tag{3.3}$$

where α_3 is dependent on S and M; for example, $\alpha_3 \approx 0.1$ when $S = 1$ cm (Thompson & Turner 1975) and $\alpha_3 \approx 0.25$ when $S = 4$ cm (Hopfinger & Toly 1976). Typical h/L_H values were close to 5.

An extensive set of measurements of u_H and w_H were made by oscillating the present grid in homogeneous water for different S and f. A laser-Doppler anemometer was used to measure the velocity components; the integral lengthscale was calculated using the measured integral timescale Γ as $L_H = u_H \Gamma$; see DeSilva & Fernando (1992). The results were found to be in good agreement with (3.1)–(3.3), with $\alpha_1 \approx 0.25$, $\alpha_2 \approx 1.25$ and $\alpha_3 \approx 0.17$; these measurements were used in data handling.

4. Experimental results

4.1. *Qualitative observations*

Because of refractive-index matching and the nature of the optical diagnostic techniques used for concentration measurements, it was not possible to use conventional shadowgraph or dye-tracer techniques to visualize the flow. The laser-

induced fluorescence technique as well as conductivity measurements, however, provided useful information on the structure of the density interface and mixing mechanisms.

Although the experiments were started with three layers, soon a fourth layer (interfacial layer) was found to develop between the turbulent and inversion layers, see figure 2(*b–d*). This particular observation is not new, and has been reported during previous investigations on mixing in two-layer and linearly stratified fluids (e.g. see Crapper & Linden 1974). The buoyancy gradient N_L in this layer is substantially larger ($N_L > N_i > N_u$), and naturally it is expected to have a significant influence on interfacial mixing. The properties of this layer (e.g. its thickness), as soon as it is formed, are also dependent on N_i, N_u, L_H, u_H, and h, and hence the governing parameters for the problem are still given by (1.2). As the flow evolves, however, N_L also plays an important role, and, if the dependent quantities are assumed to be governed by instantaneous governing variables, it is expected that the flow will be determined by N_i, N_u, L_H, u_H, h, and N_L. Some of the above variables can be eliminated based on physical arguments and experimental observations; for example, if the wave radiation into the deep stratified layer is not important N_u can be neglected. Henceforth, the following terminology will be used in describing these layers:

$$N(z) = \begin{cases} 0 & \text{for} \quad 0 < z < h_1 \quad \text{(turbulent layer)}, \\ N_L & \text{for} \quad h_1 < z < h_1 + \delta \quad \text{(interfacial layer)}, \\ N_i & \text{for} \quad h_1 + \delta < z < h_1 + \delta + h \quad \text{(inversion layer)}, \\ N_u & \text{for} \quad h_1 + \delta + h < z \quad \text{(outer layer)}. \end{cases}$$

Extensive observations were made by replaying the video records, focusing on event of interest and by image processing the video frames that appeared to be interesting. The observations suggest that the dominant mixing mechanisms vary considerably under different interfacial conditions; i.e. the mechanism of mixing is a function of the Richardson number Ri. At low Ri, say $Ri < 15$, the interfacial layer is relatively thick and is dominated by the scouring of heavy fluid parcels by turbulent eddies; see figure 3(*a*) (plate 1) which shows concentration-space and concentration gradient-space images of an interface with $Ri = 13$. The presence of the fine-scale structure (characterized by partially mixed fluid) above the interface indicates the presence of intense mixing. Observations show that thin fluid elements from the interface are sheared off, possibly by eddies sloshing over the interface. During their upward (lifting) motion, heavy fluid lumps may or may not be completely homogenized with the background fluid; some of these heavy unmixed or partially mixed fluid lumps fall back on to the interface and may subsequently be reentrained by the turbulent eddies. The presence of partially mixed fluid could be detected up to a distance of about $2L_H$ from the interface.

At higher Ri, say $Ri > 20$, interfacial wave activity is clearly evident, although occasional scouring events are still present. Observations show that these waves break and produce locally mixed regions near the entrainment interface, which are ultimately distorted and incorporated into the mixed layer by the eddies. Figure 3(*b*) shows concentration–space and concentration gradient–space images of an interface with $Ri = 26$; note the wave distortions at the interface. Figure 3(*c*) shows a growing wave, and scouring of it by a mixed-layer eddy. As Ri further increases, $Ri > 30$, scouring events are no longer present and the interfacial mixing appears to be solely due to local wave-breaking events. The spatial intermittency of wave-breaking events decreases with increasing Ri. At still larger Ri, possibly $Ri > 60$, wave-breaking events are rare;

the entrainment rate is thus reduced noticeably. Apparently, at such high Ri, molecular diffusion plays a significant role in transporting buoyancy across the interface, as reported by Crapper & Linden (1974); see figure 3(*d*). Calmness and the absence of sharp gradients are salient features of such interfaces.

Observations clearly indicate that the interfacial layer forms in response to turbulent mixing at the entrainment interface. As will be discussed in §4.3, the wave activity either in the inversion or the lower layer is weaker, and apparently a substantial fraction of the energy transferred into the stratified layer is imbibed by the breaking waves in the interfacial layer (i.e. interfacial layer acts as an energy sink). Fernando & Long (1983) and E & Hopfinger (1986) have reported similar observations during their experiments with two-layer and linearly stratified fluids.

4.2. *Displacement of isopycnals*

Internal waves present at different levels of the stratified layers can be studied by mapping the displacement field of isopycnals (or the concentration contours, in the present experiments), because it gives information on wave motions and local mixing. In the present work, the concentration (C) contours were defined by using the parameter $\beta = C/C_u$, where C_u is the concentration of the upper layer. In calculating isolines of β, vertical arrays of pixels from an image were scanned, from bottom to top, until the first pixel whose intensity was equal or less than the desired C was found, from which iso-C contours were constructed. Figure 4 shows a set of such contours corresponding to $\beta = 100$, 170 and 250, where $\tilde{\xi}$ and x represent the vertical and horizontal coordinates measured from an arbitrary origin; note the decrease of β and the increase of small-scale wave activity toward the turbulent region. In the present study, the interfacial-layer thickness δ was defined (rather arbitrarily) as the r.m.s. distance between the $\beta = 100$ and 250 contours (§4.3), the latter representing the level below which the wave activity shows rapid decay.

Contours of β were used to calculate the r.m.s. displacements of isoclines. Selected (spatial) records of $\tilde{\xi}$ versus x, from about 20 frames, taken within a 5 s period, were used to calculate the r.m.s. interfacial displacement $(\overline{\xi^2})^{\frac{1}{2}}$; to avoid problems associated with mixed fluid patches that occur intermittently in the interfacial layer, only the images with sparse wave breaking were used. Horizontal homogeneity and quasi-stationarity of interfacial turbulence were assumed in the calculations; these are satisfactory, in view of the facts that the measurements were taken away from the tank walls and that the timescale for the mixed-layer deepening is much larger than the averaging time. The sample sizes used for the data were found to give converging turbulent statistics. Figure 5(*a*) shows the variation of normalized r.m.s. wave amplitude $(\overline{\xi^2})^{\frac{1}{2}}/L_H$ as a function of the Richardson number Ri; $\beta = 100$ and 120 contours were used for the calculations. In the experiments reported, $\epsilon = N_u/N_i$ was kept constant but Ri_I was varied from 25 to 145. In the wave-breaking regime, $25 < Ri < 60$, the results can be represented by a power-law close to $(\overline{\xi^2})^{\frac{1}{2}}/L_H \sim Ri^{-1}$. A systematic variation of $(\overline{\xi^2})^{\frac{1}{2}}/L_H$ with Ri_I could not be found.

The above results can be recast and compared to the theoretical predictions of CH2. As was discussed in §2, CH2 calculated the normalized r.m.s. wave amplitude $(\overline{\xi^2})^{\frac{1}{2}}/h$ as a function of $N_i h/u_H$. Their results shows an initial rapid decrease of $(\overline{\xi^2})^{\frac{1}{2}}/h$ until about $N_i h/u_H = 1.5$ and then a levelling off to a constant value of about 0.6, independent of h/L_H. A problem arises, however, in comparing the theory and the experiment, because of the formation of a (fourth) interfacial layer to which the wave breaking is mainly confined. Thus, the rational choice of the 'inversion-layer thickness' consistent with CH2 would be the interfacial-layer thickness, δ. A comparison of the

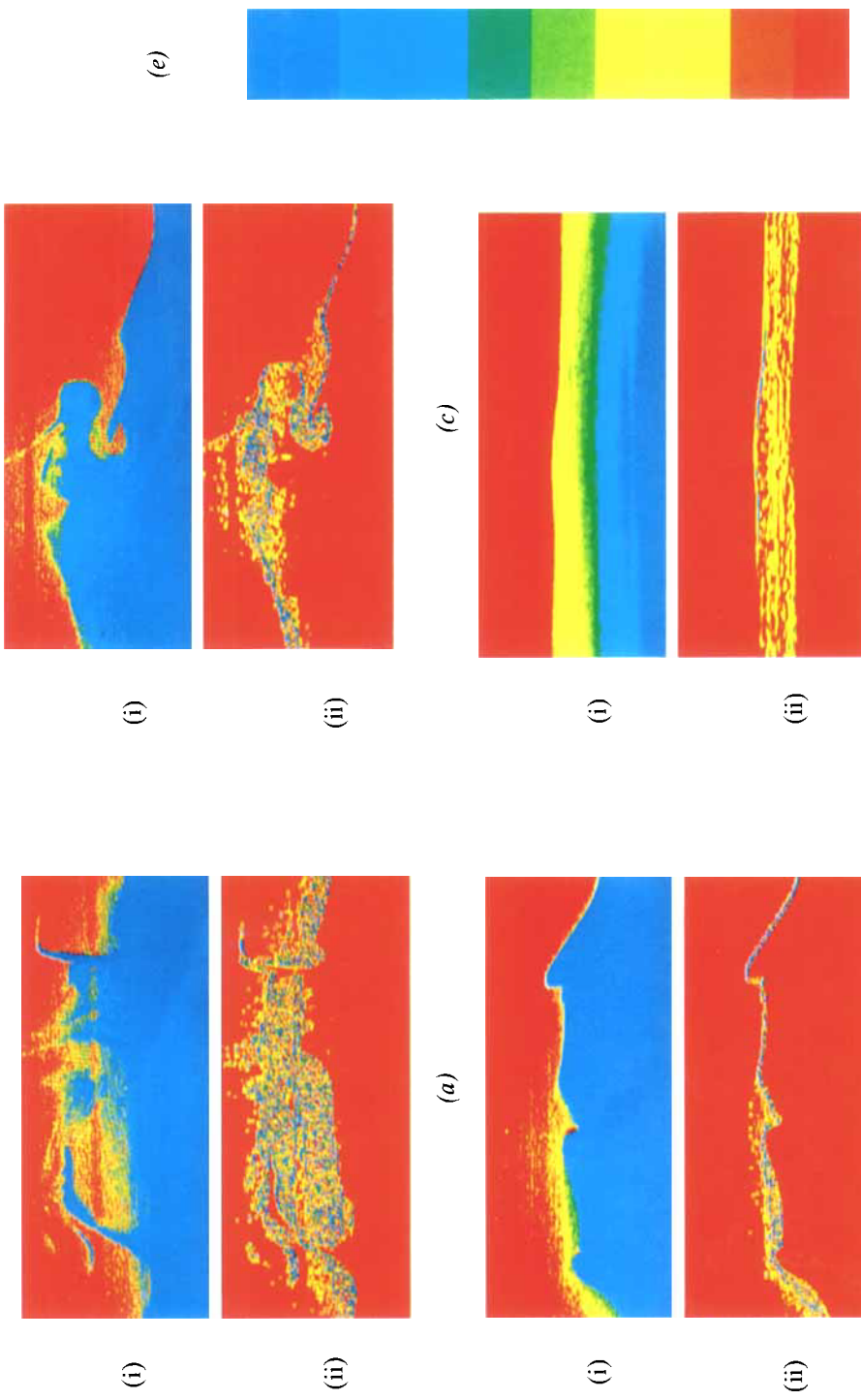

FIGURE 3. (*a*) The concentration-space (i) and concentration gradient-space (ii) images of an interface with Richardson number, $Ri = 13$. The horizontal and vertical extent of each photograph represent 6 cm and 2 cm, respectively, in real physical space; (*b*) same as in (*a*), except at $Ri = 26$; (*c*) same as in (*b*), but a wave-breaking event is shown; (*d*) same as in (*a*), except $Ri = 60$; (*e*) The false colour spectrum used for imaging.

(Facing p. 284)

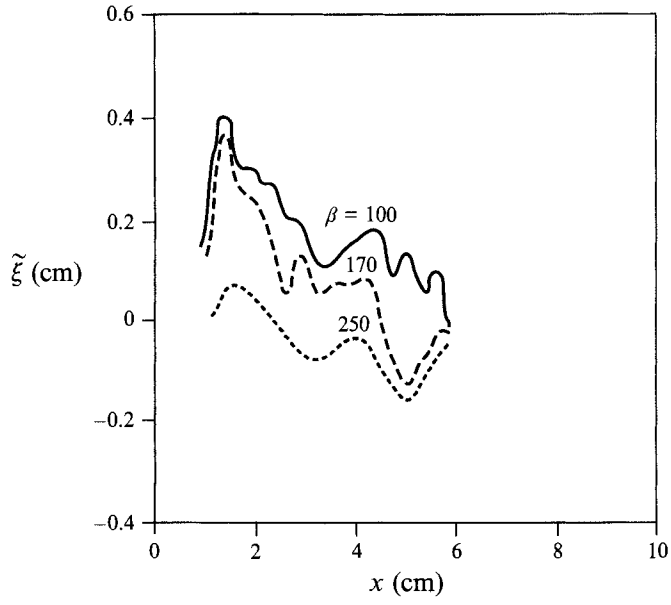

FIGURE 4. The contours of $\beta = 100$, 170 and 250 for an experiment carried out at $Ri = 20$ and $\epsilon = 0.63$. The densities corresponding to these contours are 1.0056, 1.0095 and 1.0140 (g cm^{-3}), respectively.

theoretical and experimental results is shown in figure 5(*b*); the measurement of δ will be discussed in §4.4. The agreement is not satisfactory. This was the case even if h was used as the inversion thickness.

The one-dimensional wavenumber (k_1) spectra of the interfacial distortions $\xi(x)$ were calculated using the $\beta = 100$ contour. In so doing, images that contain some wave-breaking events but well-identifiable β-contours were selected. A typical (averaged) spectrum $\psi(k_1)$ is shown in figure 6. It essentially represents the contributions to $(\overline{\xi^2})^{\frac{1}{2}}$ from the component of motions having a wavenumber k_1, in the x-direction.

Based on the work of Moffatt (1984), Fernando & Hunt (1994) proposed that breaking interfaces with sharp gradients in $\tilde{\xi}(x)$ should have a spectral region satisfying $\psi(k_1)k_1^{-2}\alpha$. This notion is consistent with the present measurements; the solid line drawn in figure 6 has a -2 slope. Additional information on the nature of interfacial motions may be obtained by considering the relationship between the wavenumber (k) and frequency (ω) of eddies. Following Tennekes (1975), CH1 proposed that the turbulent motions near the interface are governed by the advection of smaller eddies by the eddies of integral scales, namely $ku_H = \omega$. If it is assumed that the motion in the k_1 (or x) direction make the dominant contribution to the three-dimensional spectra at or near the resonant frequencies ($k_1 u_H = \omega$), k_1 corresponding to resonant modes can be estimated based on measured resonant frequencies within the interfacial layer (§4.5). The results are depicted in figure 6 as vertical arrows. Humps are evident in the averaged spectra, but they hardly represent the estimated values of k_1; at least two-dimensional spectral measurements are required before any conclusions, based on $\psi(k_1)$, can be made with regard to the eddying motions near the interface.

In addition to growing wave modes, the interface is disturbed by the eddies impinging on it; the dominant contribution for this case is expected from the energetic eddies of integral scales. The dominant horizontal scale of interfacial disturbances was

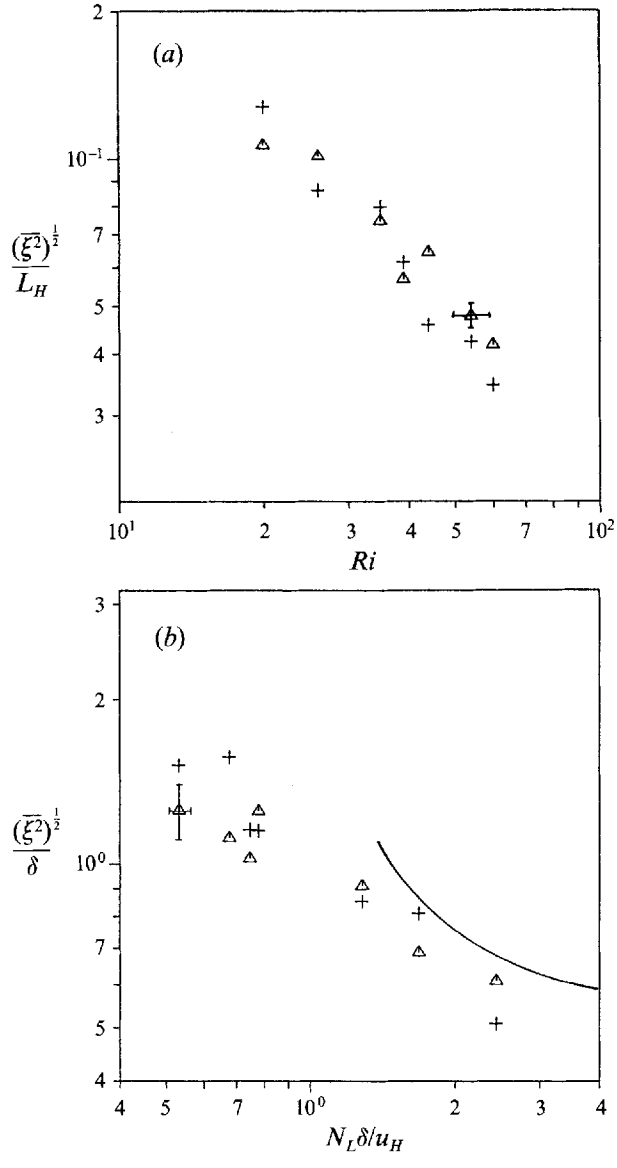

FIGURE 5. (*a*) The variation of the normalized r.m.s. interfacial distortion $(\overline{\xi^2})^{\frac{1}{2}}/L_H$ with Richardson number Ri. (*b*) A plot of $(\overline{\xi^2})^{\frac{1}{2}}/\delta$ versus $N_L\delta/u_H$, where the interfacial-layer parameter have been used for normalization; The solid line represents the CH2 prediction. The experiments correspond to $\epsilon = 0.63$, and $25 < Ri_I < 145$. +, $\beta = 100$; △, $\beta = 120$.

evaluated using variance-preserving spectral plots; i.e. peaks of $k_1\,\psi(k_1)$ versus k_1 plots. A graph of the normalized dominant wavenumber $k_d L_H$ versus Ri is shown in figure 7. In the wave-breaking regime, $Ri < 60$, $k_d L_H$ does not show a significant variation with Ri, although a slightly increasing trend cannot be ruled out for $Ri < 50$. At larger Ri, however, the magnitude of $k_d L_H$ drops, possibly, due to the change of the entrainment mechanism. Thus, in the wave-breaking regime, the dominant horizontal wavelengths are determined by the eddies whose sizes are proportional to the integral lengthscale of turbulence.

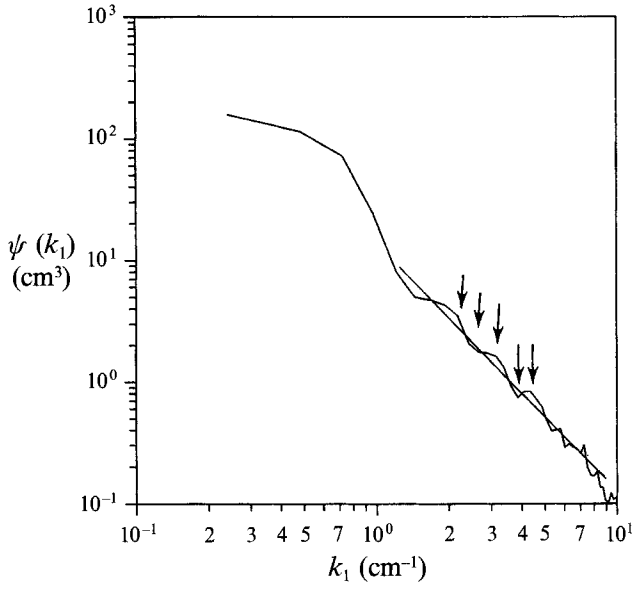

FIGURE 6. The wavenumber spectrum of interfacial distortions taken during an experiment performed with $Ri = 25$, $\epsilon = 0.63$ and $Ri_I = 182$. The arrows indicate the estimated resonant wave numbers (see text).

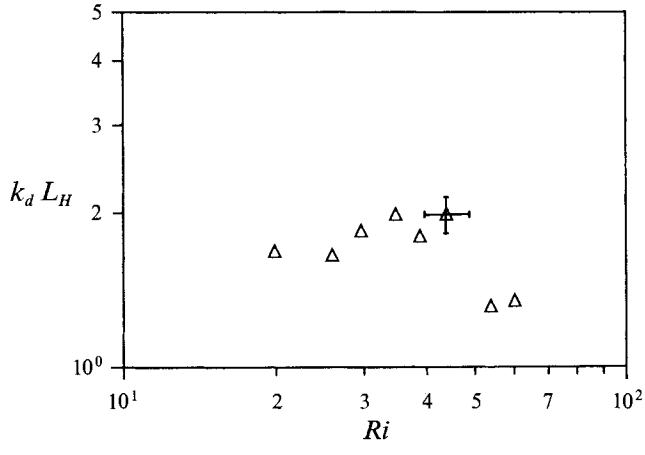

FIGURE 7. The variation of the normalized dominant wavenumber $k_d L_H$ with Ri; $\epsilon = 0.63$.

4.3. *Measurement of interfacial velocity*

Successive video frames acquired by the image processing system were used to calculate the vertical velocities of different β-contours. The elevation of a selected β-contour, say $\tilde{\xi}(x, t)$, above the x-axis was monitored in successive frames with a time separation Δt. The instantaneous vertical velocity at each point along the contour was determined using $w_i = [\tilde{\xi}(x, t+\Delta t) - \tilde{\xi}(x, t)/\Delta t$; the r.m.s. value was then calculated. The x-variation of the instantaneous velocity, calculated using three different contours of successive frames, is given in figure 8. The Ri dependence of the r.m.s. vertical velocity $(\overline{w^2})^{\frac{1}{2}}$, measured using the $\beta = 100$ and 120 contours, is shown in figure 9(a). The data in the wave-breaking regime show a power-law dependence close to $(\overline{w^2})^{\frac{1}{2}}/u_H \sim Ri^{-1}$. At low Ri (< 25), the interfacial vertical velocity is of the same order as the r.m.s.

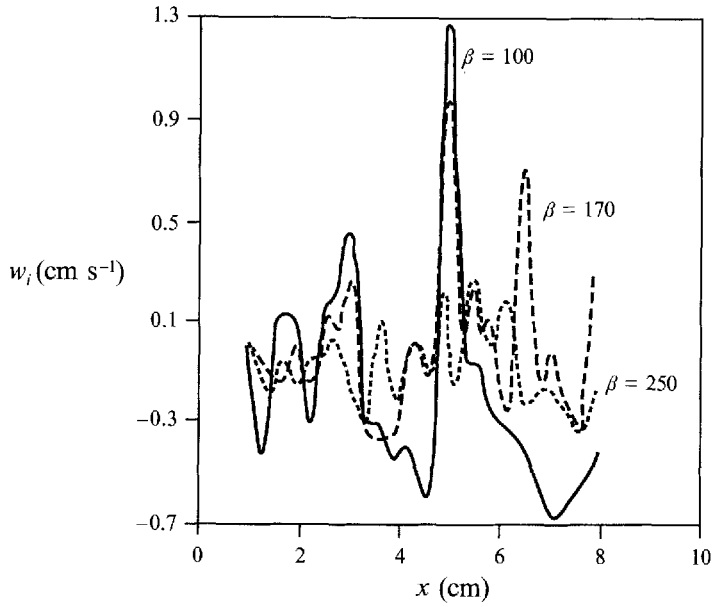

FIGURE 8. The (one-dimensional) spatial distribution of the normalized instantaneous interfacial vertical velocity calculated using three different concentration contours, $\beta = 100$, 170 and 250. The densities corresponding to these contours are 1.0056, 1.0095 and 1.0140 (g cm^{-3}), respectively; $Ri = 25$, $e = 0.63$ and $Ri_I = 182$.

velocity of the undistorted turbulence. At high Ri ($\gtrsim 60$), the interfacial velocity is smaller, possibly owing to the damping of interfacial waves under the influence of molecular-diffusive effects. Also shown in the figure are the atmospheric field data from Caughey & Palmer (1979). These are of the same order of magnitude as the laboratory measurements, but higher than that expected based on laboratory results.

The predictions of CH2 indicate an increasing trend of $(\overline{w^2})^{\frac{1}{2}}/u_H$ with $N_i h/u_H$ ($= Ri_I^{\frac{1}{2}}$) in the range $0.25 < Ri_I < 9$. A plot of the variation of $(\overline{w^2})^{\frac{1}{2}}/u_H$ with $N_L \delta/u_H$ is shown in figure 9(*b*), for the same runs as figure 9(*a*); although the predicted trend can be observed, the magnitudes of the measured velocities are smaller. The behaviour of $(\overline{w^2})^{\frac{1}{2}}/u_H$ with Ri_I based on the inversion thickness h did not show agreement with the CH2 theory, either.

The distribution of the r.m.s. vertical velocity in the stratified layer adjacent to the turbulent layer also can be obtained as described above. Since β is indicative of the (undisturbed) vertical location of a given isopycnal, velocities so calculated represent the vertical distribution of the vertical velocity. The measurements are depicted in figure 10. Note that $\beta = 100$ is indicative of the entrainment interface and $\beta = 250$ corresponds to the level where the buoyancy profile approaches the stratification of the inversion layer. Note that $\overline{w^2}$ tends to have a maximum within the interfacial layer, indicating the presence of higher modes of internal waves. This observation is in good agreement with CH2, which predicts a maximum for $\overline{w^2}$ in the wave-trapped layer. Low values of $\overline{w^2}$ at the bottom edge of the interfacial layer suggest that the wave energy radiated to the outer layers may be small. Apparently, most of the energy absorbed into the interfacial layer is consumed within it to produce turbulence by wave breaking (which eventually supports the buoyancy flux and dissipates as heat) and to overcome internal friction between various modes of waves (e.g. McEwan 1983).

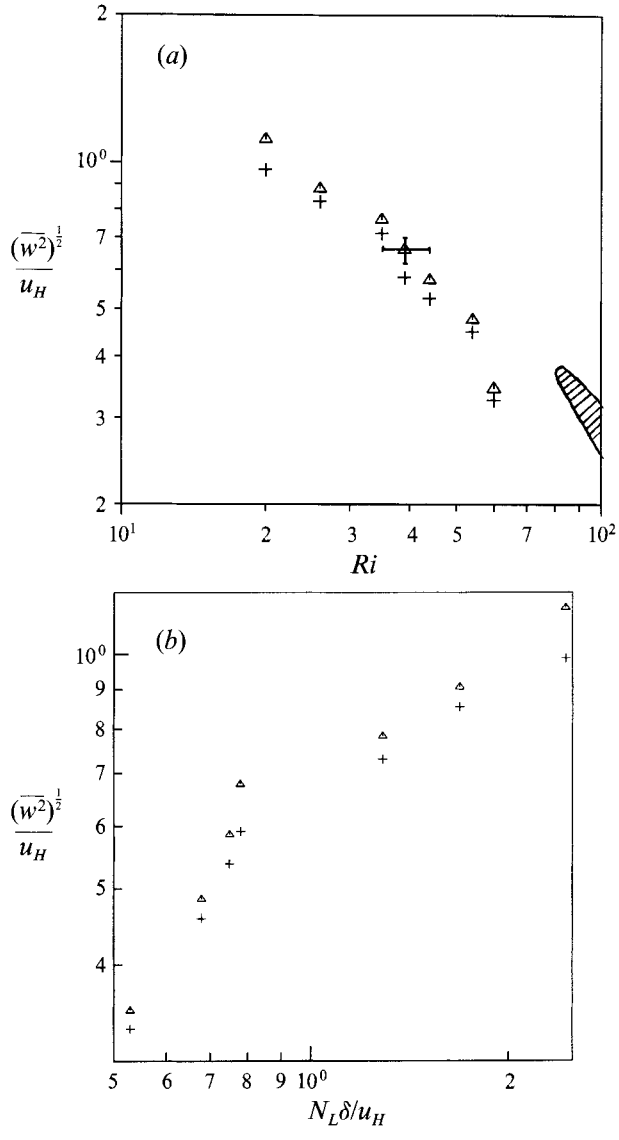

FIGURE 9. (*a*) Variation of the normalized r.m.s. interfacial velocity with the Richardson number Ri. Cross-hatched area represents the atmospheric data from Caughey & Palmer (1979). (*b*) Variation of the normalized r.m.s. interfacial vertical velocity with $N_L\delta/u_H$. The experiments correspond to $\epsilon = 0.63$ and $25 < Ri_I < 145$. +, $\beta = 100$, △, $\beta = 120$.

4.4. *Measurement of the interfacial-layer thickness*

The interfacial-layer thickness is considered as a signature of interfacial mixing events because it is formed in response to local instabilities and distortions at the entrainment interface. Inspection of the interfacial structure (figure 3) clearly reveals its complexity, and spatial and temporal variability. Considering the presence of a variety of mixing mechanisms, one should also expect different interfacial characteristics at different Ri ranges.

Observations show that when $Ri < 15$ or so, the eddies tend to penetrate into the stratified layer and agitate it, thus disturbing and partially mixing a thick region along the entrainment interface; the partially mixed fluid that has not been incorporated into

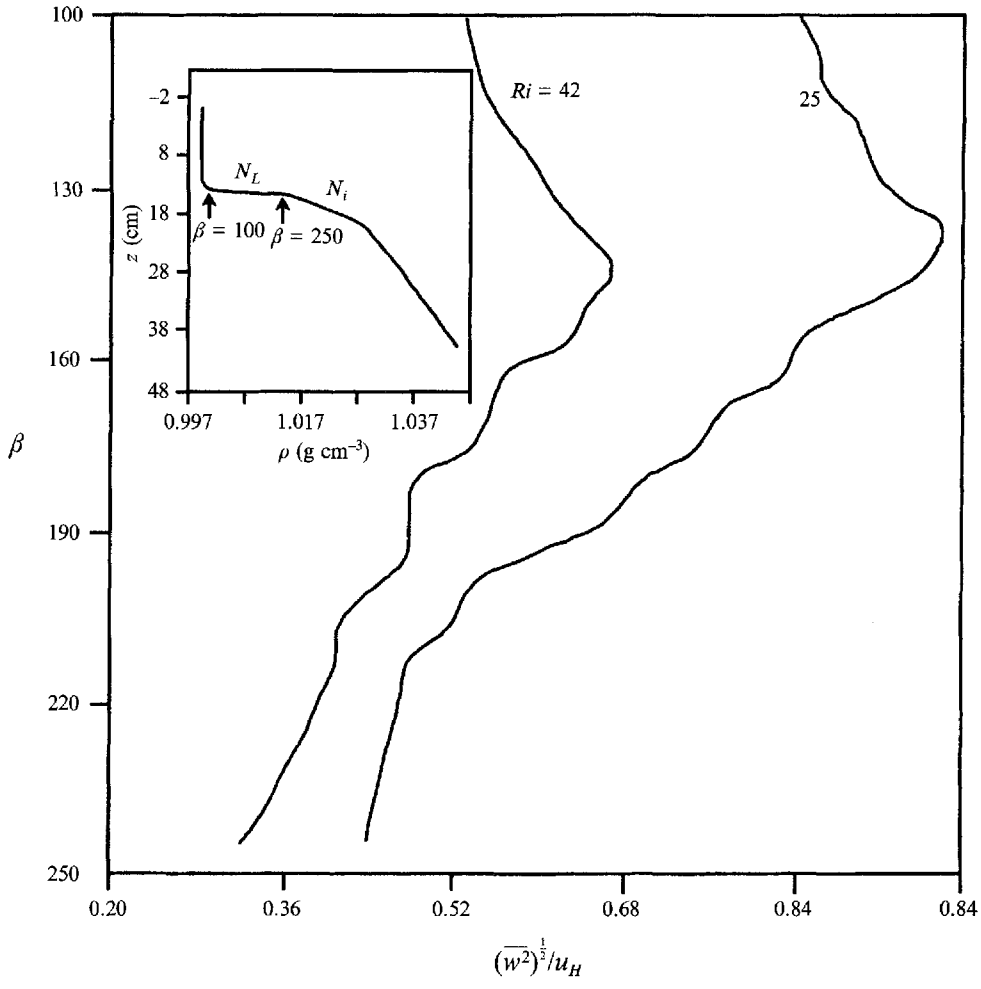

FIGURE 10. Normalized r.m.s. interfacial vertical velocities at different β-contours. The locations of $\beta = 100$ and 250 relative to the density contour for the $Ri = 25$ case are shown in the insert.

the turbulent layer may appear as the interfacial layer. At intermediate Ri, where mixing is dominated by wave breaking, isolated mixed patches are generated at the entrainment interface. Apparently, the interaction between the intrusive gravity currents that are formed during the collapse of these patches are responsible for the formation of a layer of intermediate density along the entrainment interface. Whether or not the fluid from this layer can be lifted into the mixed layer directly by the eddies is dependent on the density of the mixed fluid and the sizes of the patches (Hannoun & List 1988). At large Ri the wave breaking is absent and, according to Noh & Fernando (1993), the interfacial-layer structure is dominated by the thickening of the entrainment interface by molecular diffusion and the engulfment of the 'diffused' fluid layer by turbulent eddies.

The results for the interfacial-layer thickness δ measurements taken using the LIF technique are shown in figure 11 (δ was defined as the r.m.s. distance between the $\beta = 100$ and 250 contours); a decreasing trend of normalized δ with Ri as $\delta/L_H \sim Ri^{-2}$ can be seen in the wave-breaking regime, $20 < Ri < 60$. Hannoun & List (1988) found a similar result in their two-layer experiments, when the measurements were taken

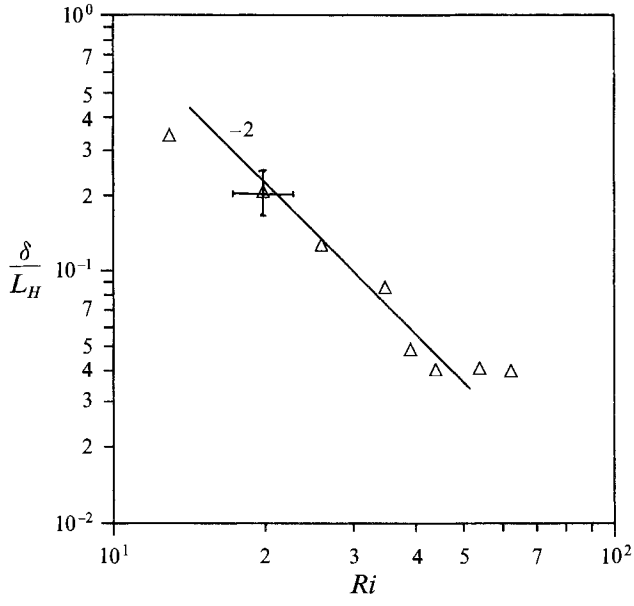

FIGURE 11. Normalized interfacial-layer thickness δ/L_H (evaluated using the LIF technique) versus Richardson number *Ri*.

along a single vertical line using LIF. In making comparisons of the present measurements with CH2, δ has been used as the thickness of the wave-breaking layer.

4.5. *Excitation of waves by turbulence*

Waves excited in stratified layers by turbulent forcing can have a range of frequencies and wavenumbers. As pointed out by Carruthers & Moeng (1987) and CH2, however, only a few selected waves can be amplified and break. For forcing frequencies (ω) smaller than N_u, the wave energy can be radiated through both layers, with some reflection occurring at the interfaces between different layers. When $N_u < \omega < N_i$, the waves can be sustained only in the inversion, and they are evanescent in the lower layer. As a consequence, some waves are trapped within the inversion and resonance is possible when the reflected waves constructively interfere with the newly generated waves at the entrainment interface.

Figure 12(*a*) shows a set of variance-preserving frequency spectra of conductivity fluctuations $\omega\psi(\omega)$ obtained from Probes C1–C4 shown in figure 1(*b*), five minutes after the start of the experiment. Strong wave/turbulence activity can be seen from Probe C1 placed in the interfacial layer. Probe C2, located at the middle of the inversion, indicates some wave activity but the wave amplitudes are smaller. Similar observations can be made from C3 and C4. It appears that a substantial amount of wave energy is trapped within the interfacial layer, with a selected number of modes bearing higher energy levels.

Figure 12(*b*) shows similar spectra taken two hours after the start of the experiment. For clarity, only the records taken from C1 and C3 are shown. A trend similar to that of figure 12(*a*) can be seen and the energy levels have not been drastically altered. These observations, together with those made using the LIF technique (which show that wave breaking is confined to the interfacial layer), suggest that there is no wave-energy build up in the inversion, which can be attributed to the dissipation of internal-wave energy by the internal friction.

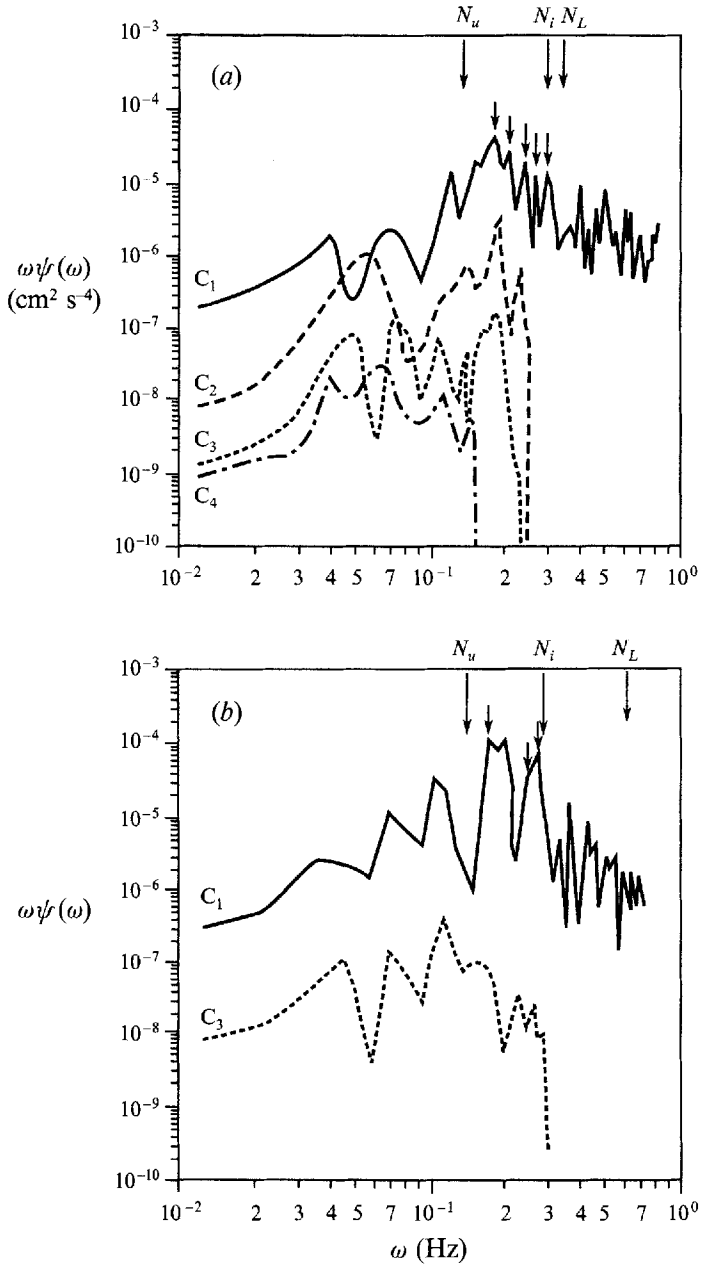

FIGURE 12. (*a*) The variance-preserving spectra of buoyancy fluctuations based on the stationary-conductivity-probe measurements. The position of the probes are given in figure 1(*b*). The data were taken 5 minutes after the initiation of grid oscillations; $\epsilon = 0.47$; $Ri = 20$. (*b*) Same as (*a*), except the data were obtained two hours after the initiation of grid oscillations.

The present experimental results can be compared to the predictions of CH2 and Carruthers & Moeng (1987). Accordingly, the resonant (amplifying) modes in the inversion (thickness h) should satisfy the criterion

$$\cot(m_1 h) = -\frac{\gamma}{m_1} + \frac{m_1^2 + \gamma^2}{m_1(k_h + \gamma)}, \tag{4.1}$$

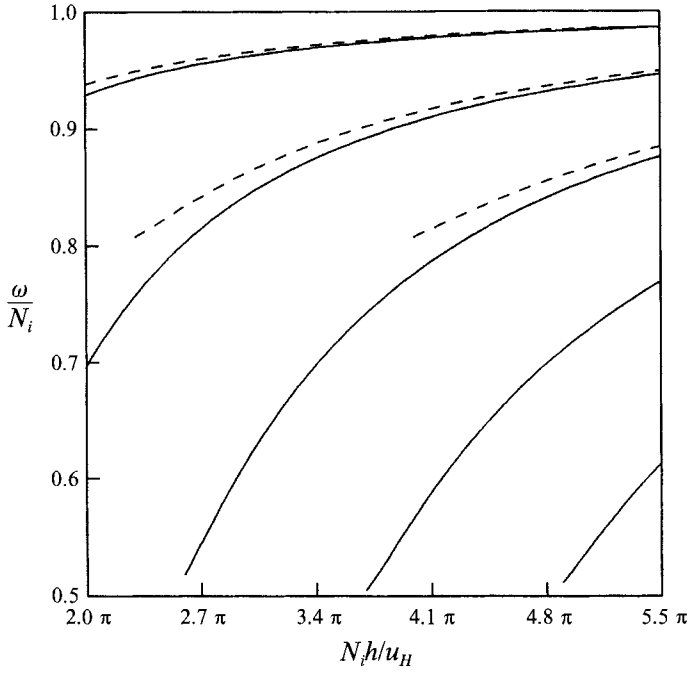

FIGURE 13. The normalized wave frequency ω/N_i versus $N_i h/u_H$. The solutions of (4.1)–(4.3) for trapped waves as a function of ϵ: ——, $\epsilon = 0.5$; – – –, $\epsilon = 0.8$.

where m_1 is the vertical wavenumber defined as

$$m_1^2 = \left(\frac{N_i^2}{\omega^2} - 1\right) k_h^2, \tag{4.2}$$

and

$$\gamma^2 = \left(1 - \frac{N_u^2}{\omega^2}\right) k_h^2, \tag{4.3}$$

where k_h is the horizontal wavenumber of turbulent eddies.

Assuming that resonant waves dominate motions in the inversion, the normalized vertical wavelength and frequency ω/N_i can be obtained from (4.1)–(4.3) as a function of $N_i h/u_H$ and the ratio $\epsilon = N_u/N_i$; the calculations are shown in figure 13. The dominant wave frequencies calculated on this basis for the present experiments are also indicated in figures 12(*a*), (*b*); for figure 12(*a*), $N_L h/u_H = 5.2\pi$ and for figure 12(*b*), $N_L h/u_H$ has dropped to 3.1π. The measured (at least the number of) dominant frequencies agree reasonably well with the calculations of CH2. The calculation of wave frequencies in CH2 using linear theory has invoked only a few assumptions, and this may be the reason for the observed agreement. Because of the inherent nonlinear nature of the problem, the calculation of wave amplitudes and velocities in the saturated wave field involves many more assumptions, as was discussed in §2; consequently, some of the predictions did not show good quantitative agreement with the laboratory observations.

Note that the probe placed within the interfacial layer has recorded additional frequencies, some of which are even greater than its own buoyancy frequency. A possible reason may be the presence of intermittent turbulence within the interfacial

layer and the exposure of the probe to the upper-layer turbulence during interfacial oscillations. Measurements made outside the interfacial layer did not indicate the presence of turbulence and the spectra showed a rapid decay beyond the local buoyancy frequency.

4.6. *Mixing at the inversion*

One of the most important consequences of wave–turbulence interactions at an inversion layer is interfacial mixing, which leads to an increase of the mixed-layer depth. In general one should expect that the rate of entrainment at the interface $u_e = \mathrm{d}h_1/\mathrm{d}t$, for the configuration shown in figure 1, to depend on u_H, L_H, h, N_i and N_u, or, on the basis of (1.2),

$$u_e/u = E = E(Ri, \epsilon, Ri_J), \tag{4.4}$$

where E is the entrainment coefficient.

However, in the experiments, an interfacial layer is developed and hence the rate of entrainment should depend on time. In addition, quantities such as the buoyancy frequency of the interfacial layer and the buoyancy jump across it also depend on the same parameters. Thus, after some rearrangement of variables, it can be shown that the entrainment coefficient can be written in terms of instantaneous local conditions at the interface as

$$E = E(Ri_\Delta, \epsilon, Ri, Ri_J), \tag{4.5}$$

where $Ri_\Delta = \Delta b L_H/u_H^2$ is the Richardson number based on the interfacial buoyancy jump. Note that the form (4.5) is convenient when comparing the present experiments to the two-layer or uniformly stratified experiments. Owing to practical difficulties, it was not possible to carry out experiments with varying Ri_Δ while keeping the other independent parameters fixed. A plot of E versus Ri_Δ, for a range of initial conditions, is shown in figure 14. The results are somewhat scattered and it is difficult to deduce the dependence of E on the governing parameters. The best-fit line to the data follows $E \propto Ri_\Delta^{-n}$, $n = 1.29$, in the wave-breaking regime. A noteworthy observation is that, for a given Ri_Δ, the entrainment rate in the present experiments is significantly smaller than that for a two-layer fluid, for example those reported by E & Hopfinger (1986); see the solid line on the figure. This is perplexing because one might expect similar entrainment rates independent of the nature of the outer stratification if the outward energy radiation is small. The observed difference may thus be attributed to the differences in the structure of the wave field at or around the entrainment interface, as pointed out in CH2. Accordingly, the resonant frequency (and hence the time available for mixing) and the interfacial energetics are dependent on the structure of the interface, as is the rate of entrainment. They find a decrease of the resonant frequency with decreasing h/L_H thus allowing more time for mixing and yielding higher entrainment rates. The present flow configuration allows the formation of higher wave modes in the stratified layer, *vis-à-vis* the previous two-layer experiments where the first mode was dominant.

5. Summary and discussion

Laboratory experiments were carried out to investigate wave and turbulent mixing characteristics of a three-layer stratified fluid system, which consists of an upper turbulent layer, a strongly stratified inversion layer (of buoyancy frequency N_i and thickness h) and a deep weakly stratified bottom layer (of buoyancy frequency N_u). The upper layer was driven by oscillating-grid-induced shear-free turbulence. The aim of the experiment was to shed light on wave–turbulence encounters occurring at the

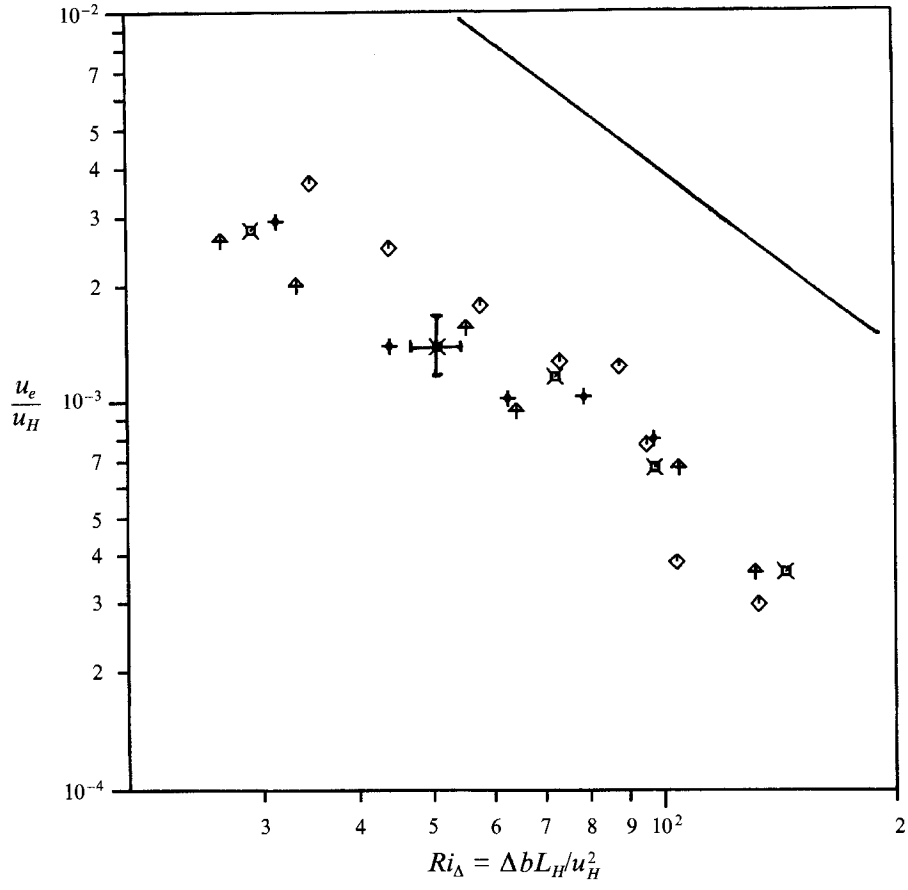

FIGURE 14. The variation of the normalized entrainment velocity u_e/u_H with the Richardson number based on the interfacial buoyancy jump Ri_Δ: $0.47 < \epsilon < 0.83$ and $25 < Ri_I < 145$. The solid line represents the data of E & Hopfinger (1986).

inversion layer of the atmospheric day-time boundary layer (during the period of strong convection), which has similar stratification and turbulence characteristics to the present experiment. To our knowledge, the three-layer configuration has not been considered in detail before in laboratory modelling, although CH2 have analysed the problem using a formal comprehensive theoretical analysis. On the other hand, turbulent mixing in initially two-layer and linearly stratified fluids has been studied extensively; for example, see Fernando (1991). CH2, however have argued that the latter cases can be dynamically different from the three-layer stratified case in view of the differences of the interfacial wave fields.

Although the experiments were started with three layers of given thicknesses, a fourth layer (interfacial layer of thickness δ) developed immediately between the inversion layer and the turbulent layer. Measurements made using the LIF technique and conductivity probes as well as flow visualization indicated that the wave activity is strongest in the interfacial layer. This observation was a persistent feature throughout the experiments, which often lasted for more than three hours. LIF flow visualization indicated the presence of different mixing mechanisms at various Ri ranges; here the Richardson number Ri is defined as $Ri = N_i^2 L_H^2 / u_H^2$, where L_H and u_H are the integral length- and velocity scales of the turbulence, respectively. When

$Ri < 15$, splashing of heavy fluid into the turbulent layer by the impinging eddies on the interface, as proposed by Linden (1973), was identified as the major mechanism: breaking of waves was dominant at $25 < Ri < 60$; and when $Ri > 60$, apparently, molecular-diffusive effects also played a role. The bulk of the measurements were taken in wave-breaking regime, from which the interfacial layer thickness δ, the r.m.s. interfacial-wave amplitude $(\overline{\xi^2})^{\frac{1}{2}}$ and the r.m.s. interfacial velocity $(\overline{w^2})^{\frac{1}{2}}$ were calculated. They were found to depend on the Richardson number as $(\overline{w^2})^{\frac{1}{2}}/u_H \approx 23\ Ri^{-1}$, $(\overline{\xi^2})^{\frac{1}{2}}/L_H \approx 2.1\ Ri^{-1}$ and $\delta/L_H \approx 90\ Ri^{-2}$. A noticeable feature was the presence of a vertical-velocity maximum within the interfacial layer, indicating the presence of higher internal-wave modes; the interfaces of most previous laboratory experiments appear to be dominated by the first mode. The dominant wavenumber of the interfacial waves k_d was found to be weakly dependent on Ri and satisfied $k_d L_H \approx 1.8$, indicating the role of long waves. The entrainment coefficient at the interface was found to follow approximately $E \propto Ri_\Delta^{-n}$, $n = 1.29$, where Ri_Δ is the Richardson number based on the buoyancy jump across the interface Δb; the dependence of E on such parameters as N_i/N_u, Ri and Ri_I was not investigated systematically, because of practical problems. For a given Ri_Δ, the observed entrainment rate in a three-layer system was significantly smaller than that of two-layer fluids. This was attributed to the differences in the internal-wave structure, which is expected to modify the energetics of the interface. Clearly, further work is necessary to understand the energetics of mixing associated with different modes of internal waves.

Attempts were made to compare the experimental results with the theory of CH2 for wave–turbulence interactions at a thick inversion layer. The measured dominant wave frequencies in the interfacial layer were found to be in fair agreement with the theory, although there are significant differences between some detailed predictions and experimental observations. One of the differences is the manner in which the 'inversion-layer thickness' is taken into consideration. Theory considers that the thickness of the wave-breaking layer is an external parameter, whereas in the experiments it is determined internally by the mixing events. The continuous modification of this layer by intermittent wave breaking is also not considered in the formulation. It appears that the theory is fully applicable at the beginning of the present experiments, but as time proceeds the interfacial region is modified by wave breaking. Also, CH2 predict wave breaking over the entire depth of the inversion layer. This is not corroborated by the present experiments, suggesting that the wave saturation criterion employed in the theory needs to be revisited.

Based on scaling arguments, Long (1978) presented a phenomenological theory for mixing in a stratified fluid by shear-free turbulence. This theory is applicable for a three-layer fluid, similar to the one studied in this paper. The prediction of this theory included $(\overline{w^2})^{\frac{1}{2}}/u_H \approx Ri^{-\frac{1}{2}}$ and $(\overline{\xi^2})^{\frac{1}{2}}/L_H \sim Ri^{-\frac{3}{4}}$, which also differ from the present findings.

The authors wish to thank the Army Research Office (Geosciences Division), Office of Naval Research (Ocean Sciences Directorate) and the National Science Foundation for financial support, and Leonard Montenegro, C. Y. Ching, Jim McGrath, and G. Oth for their help in many ways. Also the authors wish to thank Professor J.C.R. Hunt for pointing out that the discrepancy observed between the three-layer and two-layer experiments may be due to the differences in the interfacial structure.

REFERENCES

CARRUTHERS, D. J. & HUNT, J. C. R. 1986 Velocity fluctuations near an interface between a turbulent region and a stably stratified layer. *J. Fluid Mech.* **165**, 475–501 (referred to herein as CH1).

CARRUTHERS, D. J. & HUNT, J. C. R. 1994 Waves, turbulence and entrainment near an inversion layer. *J. Fluid Mech.* (submitted). (Referred to herein as CH2).

CARRUTHERS, D. J., HUNT, J. C. R. & TURFUS, C. J. 1986 Turbulent flow near density inversion layers. In *Direct and Large Eddy Simulation of Turbulence* (ed. U. Schumann & R. Friedrich), pp. 271–290. Vieweg and Son.

CARRUTHERS, D. J. & MOENG, C.-H. 1987 Waves on the overlying inversion of the convective boundary layer. *J. Atmos. Sci.* **44**, 1801–1808.

CAUGHEY, S. J., CREASE, B. A. & ROACH, W. T. 1982 A field study of nocturnal Stratocumulus *II*. *Q. J. R. Met. Soc.* **198**, 124–144.

CAUGHEY, S. J. & KITCHEN, M. 1984 Some measurements of the turbulent and microphysical structure of nocturnal stratocumulus clouds. *Q. J. R. Met. Soc.* **110**, 13–34.

CAUGHEY, S. J. & PALMER, S. G. 1979 Some aspects of turbulence through the depth of the convective boundary layer. *Q. J. R. Met. Soc.* **105**, 811–827.

CRAPPER, D. F. & LINDEN, P. F. 1974 The structure of turbulent density interface. *J. Fluid Mech.* **65**, 45–63.

DEARDORFF, J. W. 1980 Stratocumulus models derived from a three dimensional model. *Boundary-Layer Met.* **18**, 495–527.

DEARDORFF, J. W., WILLIS, G. E. & STOCKTON, B. H. 1980 Laboratory studies of the entrainment zone of a convective mixed-layer. *J. Fluid Mech.* **100**, 41–64.

DESILVA, I. P. D. & FERNANDO, H. J. S. 1992 Some aspects of mixing in a stratified turbulent patch. *J. Fluid Mech.* **240**, 601–625.

DESILVA, I P. D., MONTENEGRO, L & FERNANDO, H. J. S. 1990 Measurements of the interfacial distortions at a stratified entrainment interface. *Exp. Fluids* **9**, 13–31.

E, X. & HOPFINGER, E. J. 1986 On mixing across an interface in stably stratified fluid. *J. Fluid Mech.* **166**, 227–244.

FERNANDO, H. J. S. 1991 Turbulent mixing in stratified fluids. *Ann. Rev. Fluid Mech.* **23**, 455–493.

FERNANDO, H. J. S. & HUNT, J. C. R. 1994 Modelling of turbulent mixing at shear-free density interfaces. (Submitted for publication).

FERNANDO, H. J. S. & LONG, R. R. 1983 The growth of a grid-generated mixed layer in a two fluid system. *J. Fluid Mech.* **133**, 377–395.

FLEURY, M., MORY, M., HOPFINGER, E. J. & AUCHERE, D. 1990 Effects of rotation on turbulent mixing across a density interface. *J. Fluid Mech.* **223**, 165–191.

GOSSARD, E. E., CHADWICK, R. B., NEFF, W. D. & MORAN, K. P. 1982 The use of ground based Doppler-radar to measure gradients, fluxes and structure parameters in elevated layer. *J. Appl. Met.* **2**, 211–226.

GRISOGONO, B. & KEISLAR, R. E. 1992 Radiative stabilization of nocturnal stable atmospheric boundary layer over the desert. *Boundary-Layer Met.* **61**, 1–12.

HANNOUN, I. A., FERNANDO, H. J. S. & LIST, E. J. 1988 Turbulence structure near a sharp density interface. *J. Fluid Mech.* **189**, 189–209.

HANNOUN, I. A. & LIST, E. J. 1988 Turbulent mixing at a shear free density interface. *J. Fluid Mech.* **189**, 211–234.

HEIDT, F. D. 1977 The growth of the mixed layer in a stratified fluid due to penetrative convection. *Boundary-Layer Met.* **12**, 439–461.

HOPFINGER, E. J. & LINDEN, P. F. 1982 Formation of a thermocline in zero-mean-shear turbulence subjected to a stabilizing buoyancy flux. *J. Fluid Mech.* **114**, 157–173.

HOPFINGER, E. J. & TOLY, J.-A. 1976 Spatially decaying turbulence and its relation to mixing across density interfaces. *J. Fluid Mech.* **78**, 155–175.

KAIMAL, J. C., WYNGAARD, J. C., HAUGEN, D. A., COTE, O. R., IZUMI, Y., CAUGHEY, S. J. & READINGS, C. J. 1976 Turbulence structure in the convective boundary layer. *J. Atmos. Sci.* **33**, 2153–2169.

LINDEN, P. F. 1973 The interaction of vortex rings with a sharp density interface: a model for turbulent entrainment. *J. Fluid Mech.* **60**, 467–480.

LONG, R. R. 1978 A theory of mixing in a stably stratified fluid. *J. Fluid Mech.* **84**, 113–124.

MCEWAN, A. D. 1983 The kinematics of stratified mixing through internal wave breaking. *J. Fluid Mech.* **128**, 47–58.

MOFFAT, H. K. 1984 Simple topological aspects of turbulent vorticity dynamics. In *Proc. IUTAM Symp. on Turbulence and Chaotic Phenomena in Fluids* (ed. T. Tatsumi). Elsevier.

MOUM, J. M., CALDWELL, D. R. & PAULSON, C. A. 1989 Mixing in the equatorial surface layer and thermocline. *J. Geophys. Res.* **94** (**C2**), 2005–2021.

NOH, Y. & FERNANDO, H. J. S. 1993 The role of molecular diffusion in the deepening of the mixed layer. *Dyn. Atmos. Oceans* **17**, 187–215.

OSTER, G. & YAMAMOTO, M. 1963 Density gradient techniques. *Chem. Rev.* **63**, 257–268.

SCOTT, J. C. & KERRY, J. J. 1985 Internal waves in the bay of Biscay. Internal Report, ARE Portland.

TENNEKES, H. 1975 Eularian and Lagrangian time microscales in isotropic turbulence. *J. Fluid Mech.* **67**, 561–567.

THOMPSON, S. M. & TURNER, J. S. 1975 Mixing across an interface due to turbulence generated by an oscillating grid. *J. Fluid Mech.* 67, 349–368.

TOWNSEND, A. A. 1976 *The Structure of Turbulent Shear Flow*, pp. 232–247. Cambridge University Press.

TURNER, J. S. 1991 Convection and mixing in the oceans and the earth. *Phys. Fluids* **3**, 1218–1232.